

1 Host and viral determinants of airborne transmission of 2 SARS-CoV-2 in the Syrian hamster

3
4 Julia R. Port*¹, Dylan H. Morris², Jade C. Riopelle¹, Claude Kwe Yinda¹, Victoria A. Avanzato¹, Myndi G.
5 Holbrook¹, Trenton Bushmaker¹, Jonathan E. Schulz¹, Taylor A. Saturday¹, Kent Barbian³, Colin A.
6 Russell⁴, Rose Perry-Gottschalk⁵, Carl I. Shaia⁶, Craig Martens³, James O. Lloyd-Smith², Robert J.
7 Fischer¹, Vincent J. Munster#¹

8 1. *Laboratory of Virology, Division of Intramural Research, National Institute of Allergy and Infectious*
9 *Diseases, National Institutes of Health, Hamilton, MT, USA*

10 2. *Department of Ecology and Evolutionary Biology, University of California, Los Angeles, CA, USA*

11 3. *Rocky Mountain Research and Technologies Branch, Division of Intramural Research, National*
12 *Institute of Allergy and Infectious Diseases, National Institutes of Health, Hamilton, MT, USA*

13 4. *Department of Medical Microbiology | Amsterdam University Medical Center, University of*
14 *Amsterdam*

15 5. *Rocky Mountain Visual and Medical Arts Unit, Research Technologies Branch, Division of*
16 *Intramural Research, National Institute of Allergy and Infectious Diseases, National Institutes of*
17 *Health, Hamilton, MT, USA*

18 6. *Rocky Mountain Veterinary Branch, Division of Intramural Research, National Institute of Allergy*
19 *and Infectious Diseases, National Institutes of Health, Hamilton, MT, USA*

20
21 # Corresponding author. vincent.munster@nih.gov

23 **Author Contributions:**

24 JRP designed the studies.

25 JRP, CKY, RJF, MGH, TB, KB performed the experiments, and DHM and JLS developed and analyzed the
26 mathematical models.

27 JRP, VA, JCR, JES, CIS, KB, CM, KB, JLS, TAS analyzed results.

28 RPG generated figures.

29 JRP, DHM, JCR, JLS, VJM wrote the manuscript.

30 All co-authors reviewed the manuscript. This manuscript has been deposited as a preprint with bioRxiv
31 under a CC0 license for government authors.

32 **Competing Interest Statement:** No competing interests to disclose.

33 **Keywords:** Transmission, SARS-CoV-2, Syrian hamster, aerosols

34

35 **Summary**

36 It remains poorly understood how SARS-CoV-2 infection influences the physiological host factors important
37 for aerosol transmission. We assessed breathing pattern, exhaled droplets, and infectious virus after
38 infection with Alpha and Delta variants of concern (VOC) in the Syrian hamster. Both VOCs displayed a
39 confined window of detectable airborne virus (24h - 48h), shorter than compared to oropharyngeal swabs.
40 The loss of airborne shedding was linked to airway constriction resulting in a decrease of fine aerosols
41 produced. Male sex was associated with increased viral replication and virus shedding in the air, including
42 a VOC-independent particle-profile shift towards smaller droplets. Transmission efficiency varied among
43 donors, including a superspreading event. Co-infection with VOCs only occurred when both viruses were
44 shed by the same donor during an increased exposure timeframe. This highlights that assessment of host
45 and virus factors resulting in a differential exhaled particle profile is critical for understanding airborne
46 transmission.

47

48

49

50 **Main Text**

51 **Introduction**

52 Transmission by aerosolized virus particles has been a major contributor to the spread of SARS-CoV-2 [1,
53 2] [3-6]. Although highly efficient in preventing severe disease, vaccines do not significantly reduce
54 transmission of variants of concern (VOCs) [7]. Transmission occurs when people release respiratory
55 droplets carrying virus during (e.g.) speaking, singing, breathing, sneezing, or coughing. Droplet size and
56 half-life in the air are not uniform [8, 9] and depend on speech and breathing patterns [10], COVID-19
57 severity, and physiological parameters such as age [11, 12]. As with influenza [13], SARS-CoV-2 RNA was
58 detectable mostly in fine aerosols in humans, as opposed to coarse [11]. It is not clear how exhaled droplet
59 size, breathing patterns and even the quantity of exhaled infectious virus itself fundamentally contribute to
60 the airborne transmission efficiency *in vivo* and how COVID-19 directly influences additional physiological
61 factors which may contribute to fine aerosol production. There is reportedly large heterogeneity in the
62 transmission potential of individuals. Superspreading events have been reported numerous times
63 throughout the pandemic and are suggested to be a major driver [14, 15]. They are thought to arise from a
64 combination of biological, social, and chance factors. While human epidemiology and modeling studies
65 have highlighted various factors which may contribute to SARS-CoV-2 transmission heterogeneity,
66 including viral load [16], much of the observed variance remains poorly understood. These factors are
67 currently best studied in small animal models like the Syrian hamster, which allow for stringent and
68 controlled experimental comparisons. The Syrian hamster model has been widely used to study SARS-
69 CoV-2 transmission [17]; it recapitulates human contact, fomite and, importantly, airborne short distance
70 and fine aerosol transmission [18-21]. In this model highest efficiency of short-distance airborne
71 transmission was observed before onset of weight loss and acute lung pathology, peaking at one day post
72 inoculation and correlating to the highest virus loads in the upper respiratory tract of donor animals [22].
73 Data on lung function loss in the Syrian hamster model after SARS-CoV-2 infection is available [23, 24],
74 and virus has been demonstrated in exhaled droplets [25]. Yet, a systematic study that addresses how
75 airborne transmission potential depends on these features, along with recognized influences of sex and
76 VOC, has not been performed. The study of these contributing factors would allow us to address how they
77 come together to shape transmission outcomes.

78 Here, we introduce a mathematical model delineating for Alpha and Delta VOCs the relationship between
79 exhaled infectious virus and virus detected in the upper respiratory tract during infection and longitudinally

80 detail the changes in lung function, respiratory capacity, and exhaled particle profiles. Finally, we assess
81 the airborne transmission competitiveness and heterogeneity *in vivo* of Alpha and Delta.

82 **Results**

83 **Peak infectious SARS-CoV-2 in air samples is detected between 24 h and 48 h post infection**

84 Structural modelling and pseudotype-entry comparison suggested that the Syrian hamster model should
85 recapitulate the entry-specific competitive advantage of Delta over Alpha observed in humans (**Figure S**
86 **1A-D**). Syrian hamsters were inoculated with a low dose (10^3 TCID₅₀, intranasal (IN), N = 10 per group) of
87 SARS-CoV-2 Delta or Alpha. Animals were monitored for 14 days post inoculation (DPI). We observed no
88 significant differences in weight loss or viral titers in lung or nasal turbinates between the variants (**Figure**
89 **S 2A-C**). At 14 DPI, hamsters (N = 5) mounted a robust anti-spike IgG antibody response, and the overall
90 binding pattern was similar between Alpha and Delta (**Figure S 2D,E**). In a live virus neutralization assay,
91 homologous virus was significantly better neutralized as compared to the heterologous variant (**Figure S**
92 **2F,G**), but no significant difference was determined between the neutralization capacity against the
93 respective homologous variant (median reciprocal virus neutralization titer = 320 (Alpha anti-Alpha)/ 320
94 (Delta anti-Delta), $p = 0.9568$, N = 5, ordinary two-way ANOVA, followed by Tukey's multiple comparisons
95 test).

96 We determined the window of SARS-CoV-2 shedding for Alpha and Delta using swabs from the upper
97 respiratory tract and air sampling from cages, quantifying virus using gRNA, sgRNA, and infectious virus
98 titers. Oral swabs remained positive for gRNA and sgRNA until 7 DPI, but infectious virus dropped to
99 undetectable levels after 4 DPI in most individuals (**Figure S 3A**). Cage air was sampled during the first 5
100 days of infection in 24 h time windows from cages containing 2 or 3 animals, grouped by sex. gRNA and
101 sgRNA were detectable as early as 1 DPI in 50% of air samples and remained high through 5 DPI, while
102 infectious virus peaked at on 2 DPI and was detectable for a shorter window, from 1 to 4 DPI (**Figure S**
103 **3B**).

104

105 **Mathematical modeling demonstrates airborne shedding peaks later and declines faster than oral** 106 **swab viral load**

107 We quantified heterogeneity in shedding by variant, sex, and sampling method by fitting a mathematical
108 model of within-hamster virus kinetics (see **SI Mathematical Model**) to the data. Virus was detectable and
109 peaked earlier in oral swabs (approximately 24 h post inoculation) than virus sampled from the air
110 (approximately 48 h post inoculation), and quantity of detected virus declined slower in the swabs (**Figure**
111 **1A,B**). gRNA and sgRNA declined slower than infectious virus both in the air and in swabs. Oral swab data
112 was a poor proxy for airborne shedding, even when we directly quantified infectious virus titers. This was
113 due to a lag between peak swab shedding and peak airborne shedding. Inferred within-host exponential

114 growth and decay rates were similar for the two variants. For both variants, males shed more virus than
115 females, even after accounting for males' higher respiration rates in measurements of shedding into the air.
116 We found a slightly higher ratio of infectious virus to sgRNA in air samples for Delta than for Alpha (**Figure**
117 **1B, Figure S 3C,D**). We also found substantial individual-level heterogeneity in airborne shedding, even
118 after accounting for sex and variant (**Figure 1B**). For example, air samples from cage 5 had more than
119 twice as many peak plaques per capita than cage 6, even though both cages contained hamsters of the
120 same sex, inoculated by the same dose, route, and variant. Our model captures this, with substantial
121 inferred heterogeneity in individual airborne shedding in PFU per hour, both in timing and in height of peak
122 (**Figure 1B**)

123 **Changes in breathing profile after SARS-CoV-2 infection precede onset of weight loss and are** 124 **variant and sex-dependent**

125 Pathology in nasal turbinates and lungs did not differ significantly between animals (**Figure S 4**).
126 Pathological changes were consistent with those described previously for COVID-19 in Syrian hamsters
127 after intranasal inoculation with other SARS-CoV-2 strains [19]. Whole body plethysmography (WBP) was
128 performed. We focused the analysis on the first 5 days after inoculation, in which changes in virus shedding
129 and release into the air were observed (**Figure S 2A**). Expiratory time (T_e), inspiratory time (T_i), percentage
130 of breath occupied by the transition from inspiration to expiration (TB), end expiratory pause (EEP),
131 breathing frequency (f), peak inspiratory flow (PIFb), peak expiratory flow (PEFb), tidal volume (TVb),
132 minute volume (MVb) and enhanced pause (Penh) were used to assess changes in pulmonary function
133 throughout infection. Principal component analysis was used to determine trends in lung function changes
134 across all groups (**Figure 2A**). This revealed a large degree of inherent variation in individual hamster
135 plethysmography measures. Before inoculation there was no discernible pattern to the clustering observed
136 besides a slight separation by sex. Beginning at 2 DPI, we observed a separation of infected and control
137 animals. This coincided with the observation that all SARS-CoV-2 animals visibly decreased activity levels
138 after 2 DPI, reducing exploratory activity and grooming with sporadic short convulsions which may represent
139 coughing. No single parameter had an overwhelming influence on clustering, though several parameters
140 contributed strongly across all days: T_e , T_i , TB, EEP, f , PIFb, PEFb, TVb, and MVb (**Figure 2B,C**).

141 Broad patterns emerged by variant and by sex. Cumulative Penh AUC values for all infected groups were
142 increased compared to the sex-matched control hamsters ($p = 0.022$, Kruskal-Wallis test, $N = 5$). The
143 median Penh AUC values for Alpha, Delta, and control males were 0.741, 2.666, and 0.163, respectively
144 ($p = 0.062$). The median Penh AUC values for Alpha females, Delta females, and control females were
145 1.783, 2.255, and 0.159, respectively ($p = 0.019$). At 4 DPI, the median fold change Penh values for Alpha
146 males and Delta males were 0.793 and 1.929, respectively, as compared to 0.857 for control males. The
147 corresponding Penh values for Alpha, Delta, and control females were 1.736, 1.410, and 1.008,

148 respectively. The separation on 4 DPI did not translate to significant changes in more traditional measures
149 of respiratory function, including f, TVb, and MVb.

150 **Changes in exhaled aerosol aerodynamic profile after SARS-CoV-2 infection precede acute disease,** 151 **are variant and sex-dependent**

152 Alpha and Delta inoculated groups (N = 10 each) and a control group (N = 10) were individually evaluated
153 on 0, 1, 3, and 5 DPI. Across each variant group, particle diameter size <0.53 μm was the most abundant
154 (**Figure 3A**). No consistent, significant overall change in the number of overall particles across all sizes
155 was observed between groups (**Figure S 5C**). Particles between 1 and 10 μm in diameter, most relevant
156 for fine aerosol transmission [26], were examined. At baseline (0 DPI), females across all groups produced
157 a higher proportion of droplets in the 1-10 μm diameter range compared to males (**Figure 3A,B**). At 3 DPI,
158 the particle profiles shifted towards smaller aerodynamic diameters in the infected groups. At 5 DPI, even
159 control animals demonstrated reduced exploratory behavior, resulting in a reduction of particles in the 1-10
160 μm range, which could be due to acclimatization to the chamber. This resulted in an overall shift in particle
161 size from the 1-10 μm range to the <0.53 μm range. To analyze these data, individual slopes for each
162 animal were calculated using simple linear regression across the four timepoints (Percent ~ Intercept +
163 Slope * Day) for percent of particles in the <0.53 μm range and percent of particles in the 1-10 μm range
164 (**Figure 3C,D**), and multiple linear regression was performed. Holding variant group constant, the slope for
165 percent of particles in the 1-10 μm range was, on average, 2.2 times higher for males compared to females
166 while the <0.53 μm model estimate was 1.7 times lower. Comparing variant group while holding sex
167 constant, we found that the Delta group had a steeper decline for percent of particles in the 1-10 μm range
168 (and a steeper incline for <0.53 μm); a similar, but not as steep of a trend was observed for Alpha. After
169 adjusting for multiple comparisons using Tukey, differences in <0.53 μm slopes were observed for Delta
170 vs. Control (5.4 times higher, two-sided p = 0.0001) and Delta vs. Alpha (3 times higher, two-sided p =
171 0.0280), and for Alpha vs. Control, 2.4 times higher (two-sided p = 0.0874); for the 1-10 μm model,
172 differences were not as pronounced.

173 **Alpha and Delta VOC attack rates reveal minimal individual risk of dual infection *in-vivo***

174 We next compared attack rates between Alpha and Delta during a 4 h exposure window at 200 cm distance.
175 Groups of sentinels (N = 4 or 5) were exposed to two donor animals, one inoculated with Alpha and one
176 inoculated with Delta (**Figure 4A**).
177 sgRNA in oral swabs taken on 1 DPI varied between animals (**Figure 4B**). Sentinels were either exposed
178 first for 2 h to one variant and then for 2 h to the second (**Figure 4C**, first 4 iterations), or to both variants
179 at the same time for 4 h (last three iterations). Transmission was confirmed by sgRNA in oral swabs
180 collected from all sentinels at 2, 3, and 5 DPE. On 2 DPE, N = 13/34 sentinels were positive for sgRNA in

181 oral swabs, N = 19/34 on 3 DPE and N = 27/34 on 5 DPE. Swabs from 3 DPE and 5 DPE were sequenced,
182 and the percentage of reads mapped to Alpha, and Delta were compared (**Figure 4D,E**).

183 All animals had only one variant detectable on day 3. In total, 12 sentinels were infected with Alpha and 7
184 with Delta by 3 DPE. At 5 DPE, slightly more sentinels shed Alpha (N = 15 vs. N = 12). Interestingly, we
185 observed one superspreading event in iteration A, in which one donor animal transmitted Alpha to all
186 sentinels. For all other iterations, either both donors managed to transmit to at least one sentinel, or not all
187 sentinels were infected. For the iterations with simultaneous exposure, attack rates were similar and
188 statistically indistinguishable: Alpha = 50 %, Delta = 42.8 %. In one simultaneous exposure (iteration F),
189 three sentinels had both Delta and Alpha detectable at 5 DPE. In two, Delta was dominant, and in one
190 Alpha, always with the other variant in the clear minority (<15%). We did not observe any other such
191 coinfections (defined as a PCR positive animal with both Alpha and Delta at 5 % frequency or higher by
192 NGS). This led us to ask whether there was virus interference in sequential exposures - that is, whether
193 established infection with one variant could reduce the probability of successful infection given a later
194 exposure.

195 To assess this, we used our within-host dynamics model to calculate the estimated infection probabilities
196 for Alpha and Delta for each sentinel in each iteration, assuming each sentinel is exposed independently,
197 but accounting for the different exposure durations, donor sexes, and donor viral load (as measured by oral
198 swabs). From those probabilities, we then calculated posterior probability distributions for the number of
199 co-infections predicted to occur in each iteration if Alpha and Delta infections occurred independently and
200 did not interfere with each other (**SI Mathematical Model Figures S11-3**). We found that our observed
201 coinfections were consistent with this null model; our data do not provide clear evidence of virus interference
202 during sequential exposure, though they also do not rule out such an effect. No difference in virus replication
203 or disease severity was observed between the sentinels infected with Alpha or Delta (**Figure S 6**)
204

205 **Limited sustainability of heterologous VOC populations through multiple rounds of airborne** 206 **transmission**

207 To assess the transmission efficiency in direct competition between the Alpha and Delta VOCs, we
208 conducted an airborne transmission experiment over three subsequent rounds of exposure [21]. Donor
209 animals (N = 8) were inoculated IN with 5×10^2 TCID₅₀ of Alpha and 5×10^2 TCID₅₀ Delta (1:1 mixture) and
210 eight sentinels were exposed (Sentinels 1, 1:1 ratio) on 1 DPI for 24 h (first chain link, exposure window:
211 24-48 h post inoculation of the donors) (**Figure 5**). Two days after the start of this exposure, the eight
212 sentinels were placed into the donor side of a new cage and eight new sentinels (Sentinels 2) were exposed
213 for 24 hours (second chain link, exposure window 48-72 h post exposure start of the Sentinels 1). Again, 2
214 days after exposure start, this sequence was repeated for Sentinels 3 (third chain link, exposure window
215 48-72 h post exposure start of the Sentinels 2). All animals were individually housed between exposures,

216 and after exposure as well for the sentinels. We assessed viral presence in oropharyngeal swabs taken
217 from all animals at 2 and 5 DPI/DPE. While all Sentinels 1 demonstrated active shedding at 2 and 5 DPE,
218 in the Sentinels 2 group no viral RNA was detected in 2/8 animals and no infectious virus in 4/8 by 5 DPE.
219 In the Sentinels 3 group, sgRNA and infectious virus were only detected robustly in one animal on 5 DPE.
220 In contrast to donor animals, all infected sentinels exhibited higher shedding on day 5 compared to day 2
221 (2 DPI / 5 DPI Donors: median gRNA = 7.8 / 6.9 copies/mL (Log_{10}), median sgRNA = 7.2 / 6.4 copies/mL
222 (Log_{10}), median infectious virus titer = 2.3 / 0.5 TCID_{50} /mL (Log_{10}); Sentinels 1 (median gRNA = 7.2 / 7.4
223 copies/mL (Log_{10}), median sgRNA = 6.4 / 6.9 copies/mL (Log_{10}), median infectious virus titer = 2.9 / 2.6
224 TCID_{50} /mL (Log_{10}); Sentinels 2 = median gRNA = 3.7 / 5.4 copies/mL (Log_{10}), median sgRNA = 1.8 / 3.0
225 copies/mL (Log_{10}), median infectious virus titer = 0.5 / 1.6 TCID_{50} /mL (Log_{10})) (**Figure 5A**). Taken together,
226 this evidence suggests that the infectious shedding profile shifts later and decreases in magnitude with
227 successive generations of transmission. This could be explained by lower exposure doses causing lower
228 and slower infections in the recipients.

229 We then proceeded to compare the viral loads in the lungs and nasal turbinates at 5 DPE. Viral gRNA was
230 detected in the lungs (**Figure 5B**) and nasal turbinates (**Figure 5C**) of all Donors (lungs: median gRNA =
231 9.7 copies/gr tissue (Log_{10}), nasal turbinates: median gRNA = 6.2 copies/gr tissue (Log_{10})). Interestingly,
232 while the gRNA amount was similar in lungs between Donors and Sentinels 1 (lungs: median gRNA = 9.5
233 copies/gr tissue (Log_{10})), it was increased in nasal turbinates for the Sentinel 1 group (nasal turbinates:
234 median gRNA = 8.6 copies/gr tissue (Log_{10})). Similarly, sgRNA was increased in Sentinels 1 as compared
235 to Donors in nasal turbinates, but not lungs (Donors = lungs: median sgRNA = 9.4 copies/gr tissue (Log_{10}),
236 nasal turbinates: median sgRNA = 5.7 copies/gr tissue (Log_{10}); Sentinels 1 = lungs: median sgRNA = 9.2
237 copies/gr tissue (Log_{10}), nasal turbinates: median sgRNA = 8.4 copies/gr tissue (Log_{10})). Viral gRNA above
238 the level of quantification was detectable in 6/8 Sentinels 2 in both lungs and nasal turbinates, yet sgRNA
239 was only detected in 4/8 Sentinels 2 in lungs and 5/8 in nasal turbinates. Even though gRNA was detected
240 in 3/8 Sentinels 3, no animal had detectable sgRNA in either lungs or nasal turbinates, signaling a lack of
241 active virus replication. To confirm this, infectious virus was analyzed in both tissues for the Donors,
242 Sentinels 1, and Sentinels 2 groups (**Figure 5D**). In both tissues titers were marginally higher in Sentinels
243 1 (median TCID_{50} / gr tissue (Log_{10}) Donors: lungs = 8.6, nasal turbinates = 8.0; Sentinels 1: lungs = 8.9,
244 nasal turbinates = 8.8). Infectious virus was present in 6/8 Sentinels 2 in lungs and 5/8 in nasal turbinates.
245 Hence, even though the exposure interval for the second and third chain links were started 48 hours after
246 the start of their own exposure, not all Sentinels 2 became infected, and only one Sentinel 3 animal became
247 infected and demonstrated shedding. We conducted a separate experiment to assess viral loads in the
248 respiratory tract after SARS-CoV-2 airborne transmission at 2 DPI/DPE. While infectious virus was present
249 in oral swabs from all sentinels, virus in lungs and nasal turbinates was not present in all animals (**Figure**
250 **S 7**).

251 To determine the competitiveness of the variants, we analyzed the relative composition of the two viruses
252 using next generation sequencing (**Figure 5E,F**). Neither variant significantly outcompeted the other. We
253 first compared the percentage of Delta in oral swabs taken on 2 DPI/DPE, the day of exposure of the next
254 chain link. In Donors, no variant was more prevalent across animals or clearly outcompeted the other within
255 one host (median = 56.5% Delta, range = 40.3-69%). After the first transmission event, Delta outcompeted
256 Alpha at 2 DPE (median = 87.3% Delta, range = 19-92.7%), while after the second transmission event, half
257 (N = 2/4) the animals shed either > 80% either Alpha or Delta. Notably, and in strong contrast to the dual
258 donor experiments described above, every sentinel animal exhibited a mixed infection at 2 DPE, often with
259 proportions resembling those in the donor.

260 Next, we looked at the selective pressure within the host. By 5 DPI/DPE, no clear difference was observed
261 in Donors (median = 60 % Delta, range = 34.3-67.7%), but in the Sentinels 1 group Alpha overtook Delta
262 in three animals (median = 68.3 % Delta, range = 17-92.3%), while the reverse was never seen. In one
263 animal, we observed a balanced infection established between both variants at 5 DPE (Sentinel 1.8). In the
264 Sentinels 2 group, Alpha was the dominant variant in N = 3/8 animals, and Delta dominated in 3/8 (median
265 = 55% Delta, range = 17-92.7%). The one Sentinel 3 animal for which transmission occurred shed nearly
266 exclusively Alpha. This suggests that within one host, Alpha was marginally more successful at
267 outcompeting Delta in the oropharyngeal cavity.

268 We then assessed virus sequences in lungs and nasal turbinates to understand if the selective pressure is
269 influenced by spatial dynamics. In Donor lungs, the percentage of Alpha was marginally higher on 5 DPI
270 (median = 42.3% Delta, range = 23.3-75.7%). In the Sentinels groups, either Alpha or Delta outcompeted
271 the other variant within each animal, only one animal (Sentinel 1.8) revealing both variants > 15%. In N =
272 5/8 Sentinels 1, yet only in N = 1/4 Sentinel 2 animals, Delta outcompeted Alpha. Sequencing of virus
273 isolated from nasal turbinates reproduced this pattern. In Donors, neither variant demonstrated a complete
274 advantage (median = 51.2% Delta, range = 38.7-89.3%). In N = 5/8 Sentinels 1, and N = 3/8 Sentinels 2,
275 Delta outcompeted Alpha.

276

277 **Discussion**

278 In immunologically naïve humans, peak SARS-CoV-2 shedding is reached multiple days after exposure
279 and occurs multiple days before onset of symptoms [27]. It is not known how this informs the window of
280 transmissibility, which is poorly understood and difficult to study in the absence of controlled exposures.
281 Measuring the quantity of exhaled virus and size distribution of airborne particles is more likely to provide
282 insight into the window of transmissibility than simply measuring infectious virus in the upper respiratory
283 tract. In addition, the shedding of virus in large and fine aerosols may be a function of physiological changes
284 after infection. For hamsters, past studies have shown that SARS-CoV-2 transmissibility is limited to the
285 first three days. This coincides with peak shedding and ends before the onset of weight loss, clinical

286 manifestation, and loss of infectious virus shedding in the upper respiratory tract [2, 18, 19]. We set out to
287 determine if SARS-CoV-2 infection affects host-derived determinants of airborne transmission efficiency
288 early after infection, which may explain this restriction.

289 Human studies have found similar peak viral RNA levels for Alpha and Delta [28, 29] despite their
290 epidemiological differences, including Delta's higher transmissibility [30], shorter generation interval [31],
291 and greater risk of severe disease [32]. We observe similar kinetics in a controlled experimental setting
292 using the hamster model. We observed that viral RNA levels are a poor proxy for infectious virus, especially
293 later in infection, similar to what has been reported for humans [33]. In addition, swab samples taken from
294 the oropharynx did not directly correspond to virus sampled from air. Attempts to quantify an individual's
295 airborne infectiousness from swab measurements should thus be interpreted with caution. Similarly, viral
296 load should not be treated as a single quantity that rises and falls synchronously throughout the host; spatial
297 models of infection may be required to identify the best correlates of infectiousness [34]. Crucially, there is
298 a period early in infection (around 24 h post-infection in inoculated hamsters) when oral swabs show high
299 viral titers, but air samples exhibit low or undetectable levels of virus. It is possible that during this time
300 window the physiochemical properties of the mucus change and limit aerosol generation [26].

301 While past studies have used whole body plethysmography to differentiate the impact of VOCs on lung
302 function, these have mostly focused on using mathematically derived parameters such as P_{enh} , to compare
303 significant differences on pathology in late acute infection [24]. Within our experimental setup we observed
304 high variation within and between different hamsters. Observed differences could be contributed to the
305 behavioral state which correlated with sex, highlighting, that future studies of this nature may require
306 increased acclimatization of the animals to these experimental procedures. However, we did observe
307 changes in breathing patterns as early as 2 DPI, preceding clinical symptoms, but coinciding with the
308 window of time when infectious virus was detected in the air.

309 The majority of SARS-CoV-2 exhaled from hamsters was observed within droplet nuclei $<5 \mu\text{m}$ in size [27].
310 We report a rise in $<0.53 \mu\text{m}$ particles and a drop in particles in the 1-10 μm range after infection. One of
311 the caveats of these measurements in small animals is that detected particles may come from aerosolized
312 fomites, and residual dust generated by movement [35]. In our system, we did not detect any particles
313 originating from dead animals or the environment, but we also saw a noticeable reduction of particles across
314 sizes when movement was minimal, or animals were deeply asleep. Considering the individual variability
315 in the lung function data, we did not observe that this shift in particle production was accompanied by a
316 consistent change in either breathing frequency, tidal volume, or minute volume. Humans with COVID-19
317 have been shown to exhale fewer particles than uninfected individuals during normal breathing, but not
318 during coughing [36] and fine aerosols have been found to be the major source of virus-loaded droplets.
319 This suggests that a shorter duration of measurable infectious virus in air, as opposed to the upper
320 respiratory tract, could be partially due to early changes in airway constriction and a reduction in exhaled

321 particles of the optimal size range for transmission. The mechanisms involved in the changing aerodynamic
322 particle profile, and the distribution of viral RNA across particle sizes, require further characterization in the
323 hamster model.

324 Lastly, we compared the transmission efficiency of the Alpha and Delta variants in this system. We did not
325 find a clear transmission advantage for Delta over Alpha in Syrian hamsters, in either an attack rate
326 simulation or when comparing intra- and inter-host competitiveness over multiple generations of airborne
327 transmission. This contrasts sharply with epidemiological observations in the human population, where
328 Delta rapidly replaced Alpha (or other VOCs). The Syrian hamster model may not completely recapitulate
329 all aspects of SARS-CoV-2 virus kinetics and transmission in humans, particularly as the virus continues to
330 adapt to its human host. At the time of emergence of Delta, a large part of the human population was either
331 previously exposed to and/or vaccinated, the underlying immune status might have played a role in
332 providing additional selective pressure. Analyses of the cross-neutralization between Alpha and Delta
333 suggest subtly different antigenic profiles [37]. Two VOC with similar phenotype, as observed here for Alpha
334 and Delta, would theoretically be more likely to be transmitted as a mixed-variant population. In contrast, in
335 viruses with a differential phenotypic, such as Alpha and the Lineage A, Alpha outcompeted the Lineage A
336 virus providing a clear evolutionary basis for the emergence of Alpha [2, 38].

337 Our two transmission experiments yielded different outcomes. When sentinel hamsters were sequentially
338 exposed, first to Alpha and then to Delta, generally no dual infection were observed. In contrast, when we
339 exposed hamsters to donors simultaneously infected with Alpha and Delta, mixed variant rather than single
340 variant populations was transmitted. These mixed variant infections were not retained equally, and the
341 relative VOC frequencies differed between investigated compartments of the respiratory tract, suggesting
342 that beside immune invasion and transmission efficiency additional factors such as the innate immune
343 response impose selective pressure on the virus populations. This suggest that there are opportunities for
344 both single-virion and viral population transmission events, dictated by origin and exposure dose. During
345 brief exposures, the risk of acquiring an infection of distinct viral genotypes (and hence, the risk of
346 recombination) may be relatively low on the individual level.

347 A combination of non-static host, environmental and virus parameters such as: virus phenotype, shedding
348 in air, individual variability and sex differences, changes in breathing patterns and droplet size, likely play a
349 role in successful transmission. These host and viral parameters might explain SARS-CoV-2's over-
350 dispersed transmission pattern. SARS-CoV-2 human-to-human transmission is characterized by
351 continuous circulation in the human population, with a R_0 ranging from 1.5 to 6.68 in naïve populations [39,
352 40](Delta: R_0 of 5.08; Omicron: $R_0 = 8.2$ and $R_e = 3.6$ [41, 42]). This relatively low R_e suggests that many
353 transmission chains are self-limiting. However, relatively rare superspreading events have been reported
354 for SARS-CoV-2; heterogeneity in the respiratory viral loads is high and some infected humans release
355 tens to thousands of SARS-CoV-2 virions/min [43, 44]. Our findings recapitulate this. Quantitative

356 assessment of virus and host parameter responsible for the size, duration and infectivity of exhaled aerosols
357 may be critical in our understanding what defines successful transmission for SARS-CoV-2.

358

359 **Materials and Methods**

360 *Ethics Statement*

361 All animal experiments were conducted in an AAALAC International-accredited facility and were approved
362 by the Rocky Mountain Laboratories Institutional Care and Use Committee following the guidelines put forth
363 in the Guide for the Care and Use of Laboratory Animals 8th edition, the Animal Welfare Act, United States
364 Department of Agriculture and the United States Public Health Service Policy on the Humane Care and
365 Use of Laboratory Animals. Protocol number 2021-034-E. Work with infectious SARS-CoV-2 virus strains
366 under BSL3 conditions was approved by the Institutional Biosafety Committee (IBC). For the removal of
367 specimens from high containment areas virus inactivation of all samples was performed according to IBC-
368 approved standard operating procedures.

369

370 *Cells and viruses*

371 SARS-CoV-2 variant Alpha (B.1.1.7) (hCoV320 19/England/204820464/2020, EPI_ISL_683466) was
372 obtained from Public Health England via BEI Resources. Variant Delta (B.1.617.2/) (hCoV-19/USA/KY-
373 CDC-2-4242084/2021, EPI_ISL_1823618) was obtained from BEI Resources. Virus propagation was
374 performed in VeroE6 cells in DMEM supplemented with 2% fetal bovine serum, 1 mM L-glutamine, 50 U/mL
375 penicillin and 50 µg/mL streptomycin (DMEM2). VeroE6 cells were maintained in DMEM supplemented
376 with 10% fetal bovine serum, 1 mM L- glutamine, 50 U/mL penicillin and 50 µg/ml streptomycin. No
377 mycoplasma and no contaminants were detected. All virus stocks were sequenced; no SNPs compared to
378 the patient sample sequence were detected in the Delta stock. In the Alpha stock we detected: ORF1AB
379 D3725G: 13% ORF1AB L3826F: 18%.

380

381 *Pseudotype entry assay*

382 The spike coding sequences for SARS-CoV-2 variant Alpha and Delta were truncated by deleting 19 aa at
383 the C-terminus. The S proteins with the 19 aa deletions of coronaviruses were previously reported to show
384 increased efficiency incorporating into virions of VSV [45, 46]. These sequences were codon optimized for
385 human cells, then appended with a 5' kozak expression sequence (GCCACC) and 3' tetra-glycine linker
386 followed by nucleotides encoding a FLAG-tag sequence (DYKDDDDK). These spike sequences were
387 synthesized and cloned into pcDNA3.1+(GenScript). Human and hamster ACE2 (Q9BYF1.2 and
388 GQ262794.1, respectively) were synthesized and cloned into pcDNA3.1+ (GenScript). All DNA constructs
389 were verified by Sanger sequencing (ACGT). BHK cells were seeded in black 96-well plates and transfected

390 the next day with 100 ng plasmid DNA encoding human or hamster ACE2, using polyethylenimine
391 (Polysciences). All downstream experiments were performed 24 h post-transfection. Pseudotype
392 production was carried out as described previously [47]. Briefly, plates pre-coated with poly-L-lysine
393 (Sigma–Aldrich) were seeded with 293T cells and transfected the following day with 1,200 ng of empty
394 plasmid and 400 ng of plasmid encoding coronavirus spike or no-spike plasmid control (green fluorescent
395 protein (GFP)). After 24 h, transfected cells were infected with VSVΔG seed particles pseudotyped with
396 VSV-G as previously described [47, 48]. After one hour of incubating with intermittent shaking at 37 °C,
397 cells were washed four times and incubated in 2 mL DMEM supplemented with 2% FBS,
398 penicillin/streptomycin, and L-glutamine for 48 h. Supernatants were collected, centrifuged at 500xg for
399 5 min, aliquoted, and stored at –80 °C. BHK cells previously transfected with ACE2 plasmids of interest
400 were inoculated with equivalent volumes of pseudotype stocks. Plates were then centrifuged at 1200xg at
401 4 °C for one hour and incubated overnight at 37 °C. Approximately 18–20 h post-infection, Bright-Glo
402 luciferase reagent (Promega) was added to each well, 1:1, and luciferase was measured. Relative entry
403 was calculated by normalizing the relative light unit for spike pseudotypes to the plate relative light unit
404 average for the no-spike control. Each figure shows the data for two technical replicates.

405

406 *Structural interaction analysis*

407 The locations of the described spike mutations in the Alpha and Delta VOCs were highlighted on the SARS-
408 CoV-2 spike structure (PDB 6ZGE, [49]). To visualize the molecular interactions at the RBD-ACE2 binding
409 interface, the crystal structure of the Alpha variant RBD and human ACE2 complex (PDB 7EKF [50]) was
410 utilized. All figures were generated using The PyMOL Molecular Graphics System
411 (<https://www.schrodinger.com/pymol>).

412

413 *Hamster infection with Alpha and Delta*

414 Four-to-six-week-old female and male Syrian hamsters (ENVIGO) were inoculated (10 animals per virus)
415 intranasally (IN) with either SARS-CoV-2 strain England/204820464/2020 (B.1.1.7/Alpha,
416 EPI_ISL_683466), hCoV-19/USA/KY-CDC-2-4242084/2021 (B.1.617.2/Delta, EPI_ISL_1823618), or no
417 virus (anesthesia controls). IN inoculation was performed with 40 µL sterile DMEM containing 10³ TCID₅₀
418 SARS-CoV-2 or simply sterile DMEM. At five days post inoculation (DPI), five hamsters from each group
419 were euthanized and tissues were collected. The remaining 5 animals were euthanized at 14 DPI for
420 disease course assessment and shedding analysis. For the control group, no day 5 necropsy was
421 performed. Hamsters were weighed daily, and oropharyngeal swabs were taken on day 1, 2, 3, 4, 5, and
422 7. Swabs were collected in 1 mL DMEM with 200 U/mL penicillin and 200 µg/mL streptomycin. For the
423 control group, mock swabs were performed to ensure animals underwent the same anesthesia protocols
424 as infection groups. On day -1, 0, 1, 2, 3, 4, 5, 6, 7, and 14 whole body plethysmography was performed.

425 Profiles of particles produced by hamsters were collected on day 0, 1, 3, and 5. Cage air was sampled on
426 day 0, 1, 2, 3, 4, and 5. Hamsters were observed daily for clinical signs of disease. Necropsies and tissue
427 sampling were performed according to IBC-approved protocols.

428

429 *Air sampling of hamster cages*

430 During the first 5 days, hamsters were housed in modified cages hooked up to an air pump. Air flow was
431 generated at 30 cage changes/h. Between the cage and the pump a 47 mm gelatin air filter was installed.
432 Filters were exchanged in 24-h intervals. The filters were dissolved in 5 mL of DMEM containing 10% FBS
433 and presence of virus was determined by qRT PCR and plaque assay.

434

435 *Aerodynamic particle sizing of exhaled droplets*

436 Two strategies were used to measure the aerodynamic diameter of droplets exhaled by hamsters. SARS-
437 CoV-2 inoculated hamsters or uninfected control animals were placed into a 1.25 L isoflurane chamber.
438 This allowed free movement of the animal in the chamber. The chamber was hooked up with one port to a
439 HEPA filter. The second port was hooked up to a Model 3321 aerodynamic particle sizer spectrometer
440 (TSI). Both chamber and particle sizer were placed into a BSC class II cabinet. Animals remained in the
441 chamber for 5 x 1 min readings. For each set of readings, there were 52 different particle sizes. For each
442 hamster and timepoint, the total number of particles was calculated and the percent of particles in a
443 particular diameter range was derived using this total. RStudio 2021.09.1 Build 372 Ghost Orchid Release,
444 R version 4.1.2 (2021-11-01), Tidyverse R package version 1.3.1 (2021-04-15), and Emmeans R package
445 version 1.7.2 (2022-01-04) were used for the aerodynamic particle size analysis.

446 To differentiate between particle profiles produced by an awake and moving animal and those produced by
447 a sleeping animal with limited movement, uninfected age-matched hamsters (3 males and 2 female) were
448 acclimatized to being inside a 38.1 mm inside diameter tube hooked up to a particle sizer (**Figure S 5A,B**).
449 Both tube and particle sizer were placed into a BSC class II cabinet. To acclimate the animals to the tube,
450 sunflower seeds were provided to encourage investigation and free entry and exit from the tube. After
451 animals became used to being in the tube, ends were capped as depicted and 5 x 5 min readings were
452 taken. The particle size was measured using a Model 3321 aerodynamic particle sizer spectrometer (TSI).
453 Particle size profiles were analyzed using TSI software. As a control, particles originating from empty
454 enclosures and euthanized animals were recorded and found to be absent

455

456 *Aerosol transmission attack rate experiment*

457 Four-to-six-week-old female and male Syrian hamsters (ENVIGO) were used. In this experiment naïve
458 hamsters (sentinels) were exposed to donors infected with either Alpha or Delta in the same aerosol

459 transmission set-up to evaluate the attack rates of both variants. Donor hamsters were infected intranasally
460 as described above with 10^3 TCID₅₀ SARS-CoV-2 (Alpha or Delta, N = 7, respectively) and housed
461 individually. After 24 h donor animals were placed into the donor cage. 4 or 5 sentinels were placed into
462 the sentinel cage (N = 34, 7 iterations), which was connected to the donor cage by a 2 m tube and exposed
463 for 4 h. Air flow was generated between the cages from the donor to the sentinel cage at 30 cage changes/h.
464 One donor inoculated with Alpha, and one donor inoculated with Delta were randomly chosen for each
465 scenario. Both donors were either placed together into the donor cage, or, alternatively, first one donor was
466 placed into the cage for 2 h, then the other for 2 h. To ensure no cross-contamination, the donor cages and
467 the sentinel cages were never opened at the same time, sentinel hamsters were not exposed to the same
468 handling equipment as donors, and equipment was disinfected with either 70% ETOH or 5% Microchem
469 after each sentinel. Regular bedding was replaced by alpha-dri bedding to avoid the generation of dust
470 particles. Oropharyngeal swabs were taken for donors after completion of the exposure and for sentinels
471 on days 2, 3, and 5 after exposure. Swabs were collected in 1 mL DMEM with 200 U/mL penicillin and 200
472 µg/mL streptomycin. Donors were euthanized after exposure ended, and sentinels were euthanized on day
473 5 for collection of lungs. All animals were always single housed outside the exposure window.

474

475 *Variant competitiveness transmission chain*

476 Four-to six-week-old female and male Syrian hamsters (ENVIGO) were used. Donor hamsters (N = 8) were
477 infected intranasally as described above with 10^3 TCID₅₀ SARS-CoV-2 at a 1:1 ratio of Alpha and Delta
478 (exact titration of the inoculum for both variants = 503 TCID₅₀, 80% Delta sequencing reads). After 12 hours,
479 donor animals were placed into the donor cage and sentinels (Sentinels 1, N = 8) were placed into the
480 sentinel cage (1:1) at a 16.5 cm distance with an airflow of 30 cage changes/h as described by Port et al.
481 [21]. Hamsters were co-housed for 24 h. The following day, donor animals were re-housed into regular
482 rodent caging. One day later, Sentinels 1 were placed into the donor cage of new transmission set-ups.
483 New sentinels (Sentinels 2, N = 8) were placed into the sentinel cage (2:2) at a 16.5 cm distance with an
484 airflow of 30 changes/h. Hamsters were co-housed for 24 h. Then, Sentinels 1 were re-housed into regular
485 rodent caging and Sentinels 2 were placed into the donor cage of new transmission set-ups one day later.
486 New sentinels (Sentinels 3, N = 8) were placed into the sentinel cage (2:2) at a 16.5 cm distance with an
487 airflow of 30 changes/h. Hamsters were co-housed for 24 h. Then both Sentinels 2 and Sentinels 3 were
488 re-housed to regular rodent caging and monitored until 5 DPE. Oropharyngeal swabs were taken for all
489 animals at 2 and 5 DPI/DPE. All animals were euthanized at 5 DPI/DPE for collection of lung tissue and
490 nasal turbinates. To ensure no cross-contamination, the donor cages and the sentinel cages were never
491 opened at the same time, sentinel hamsters were not exposed to the same handling equipment as donors,
492 and the equipment was disinfected with either 70% EtOH or 5% Microchem after each sentinel. Regular
493 bedding was replaced by alpha-dri bedding to avoid the generation of dust particles.

494

495 *Within-host kinetics model*

496 We used Bayesian inference to fit a semi-mechanistic model of within-host virus kinetics and shedding to
497 our data from inoculated hamsters. Briefly, the model assumes a period of exponential growth of virus within
498 the host up to a peak viral load, followed by exponential decay. It assumes virus shedding into the air follows
499 similar dynamics, and the time of peak air shedding and peak swab viral load may be offset from each other
500 by an inferred factor. Decay of RNA may be slower than that of infectious virus by an inferred factor,
501 representing the possibility, seen in our data, that some amplified RNA may be residual rather than
502 representative of current infectious virus levels. We also inferred conversion factors (ratios) among the
503 various quantities, i.e., how many oral swab sgRNA copies correspond to an infectious virion at peak viral
504 load. We fit the model to our swab and cage air sample data using Numpyro [51], which implements a No-
505 U-Turn Sampler [52]. For full mathematical details of the model and how it was fit, including prior distribution
506 choices and predictive checks, see the **SI Mathematical Model**.

507

508 *Aerosol caging*

509 Aerosol cages as described by Port *et al.* [21] were used for transmission experiments and air sampling as
510 indicated.

511

512 *Whole body plethysmography*

513 Whole body plethysmography was performed on SARS-CoV-2 and uninfected Syrian hamsters. Animals
514 were individually acclimated to the plethysmography chamber (Buxco Electronics Ltd., NY, USA) for 20
515 minutes, followed by a 5-minute measurement period with measurements taken continuously and averaged
516 over two-second intervals. Initial data was found to have an especially high rejection index (Rinx) for
517 breaths, so was reanalyzed using a custom Buxco formula to account for differences between mice and
518 hamsters. This included expanding the acceptable balance range, the percent change in volume between
519 inhalation and exhalation, from 20-180% to 15-360%. Reanalysis using this algorithm resulted in the Rinx
520 across all hamsters from one day before infection to 5 days post-infection decreasing from 62.97% to
521 48.65%. The reanalyzed data were then used for further analysis. Each hamster's individual averages one
522 day prior to infection were used as their baselines for data analysis.

523 Areas under the curve (AUCs) for each parameter were calculated for each individual hamster based on
524 their raw deviation from baseline at each time point. Either positive or negative peaks were assessed based
525 on parameter-specific changes. Principal component analyses (PCAs) to visualize any potential clustering
526 of animals over the course of infection were performed for each day on raw values for each of the
527 parameters to accurately capture the true clustering with the least amount of data manipulation. PCAs and

528 associated visualizations were coded in R using RStudio version 1.4.1717 (RStudio Team, 2021). The
529 readxl package version 1.3.1 was then used to import Excel data into RStudio for analysis (Wickham and
530 Bryan, 2019). Only parameters that encapsulated measures of respiratory function were included (zero-
531 centered, scaled). The factoextra package version 1.0.1 (Kassambara and Mundt, 2020) was used to
532 determine the optimal number of clusters for each PCA via the average silhouette width method and results
533 were visualized using the ggplot2 package (Wickham, 2016). Correlation plots were generated based on
534 raw values for each lung function parameter using the corrplot package version 0.90 (Wei and Simko,
535 2021). The color palette for correlation plots was determined using RColorBrewer version 1.1-2 (Neuwirth,
536 2014).

537

538 *Viral RNA detection*

539 Swabs from hamsters were collected as described above. 140 μ L was utilized for RNA extraction using the
540 QIAamp Viral RNA Kit (Qiagen) using QIAcube HT automated system (Qiagen) according to the
541 manufacturer's instructions with an elution volume of 150 μ L. For tissues, RNA was isolated using the
542 RNeasy Mini kit (Qiagen) according to the manufacturer's instructions and eluted in 60 μ L. Sub-genomic
543 (sg) and genomic (g) viral RNA were detected by qRT-PCR [53, 54]. RNA was tested with TaqMan™ Fast
544 Virus One-Step Master Mix (Applied Biosystems) using QuantStudio 6 or 3 Flex Real-Time PCR System
545 (Applied Biosystems). SARS-CoV-2 standards with known copy numbers were used to construct a standard
546 curve and calculate copy numbers/mL or copy numbers/g.

547

548 *Viral titration*

549 Viable virus in tissue samples was determined as previously described [15]. In brief, lung tissue samples
550 were weighed, then homogenized in 1 mL of DMEM (2% FBS). Swabs were used undiluted. VeroE6 cells
551 were inoculated with ten-fold serial dilutions of homogenate, incubated for 1 hour at 37°C, and the first two
552 dilutions washed twice with 2% DMEM. For swab samples, cells were inoculated with ten-fold serial
553 dilutions and no wash was performed. After 6 days, cells were scored for cytopathic effect. TCID₅₀/mL was
554 calculated by the Spearman-Kärber method. To determine titers in air samples, a plaque assay was used.
555 VeroE6 cells were inoculated with 200 μ L/well (48-well plate) of undiluted samples, no wash was performed.
556 Plates were spun for 1 h at RT at 1000 rpm. 800 μ L of CMC (500 mL MEM (Cat#10370, Gibco, must contain
557 NEAA), 5 mL PenStrep, 7.5 g carboxymethylcellulose (CMC, Cat# C4888, Sigma, sterilize in autoclave)
558 overlay medium was added to each well and plates incubated for 6-days at 37°C. Plates were fixed with
559 10% formalin overnight, then rinsed and stained with 1% crystal violet for 10 min. Plaques were counted.

560

561 *Serology*

562 Serum samples were analyzed as previously described [55]. In brief, maxisorp plates (Nunc) were coated
563 with 50 ng spike protein (generated in-house) per well. Plates were incubated overnight at 4°C. Plates were
564 blocked with casein in phosphate buffered saline (PBS) (ThermoFisher) for 1 hours at room temperature
565 (RT). Serum was diluted 2-fold in blocking buffer and samples (duplicate) were incubated for 1 hour at RT.
566 Secondary goat anti-hamster IgG Fc (horseradish peroxidase (HRP)-conjugated, Abcam) spike-specific
567 antibodies were used for detection and KPL TMB 2-component peroxidase substrate kit (SeraCare, 5120-
568 0047) was used for visualization. The reaction was stopped with KPL stop solution (Seracare) and plates
569 were read at 450 nm. The threshold for positivity was calculated as the average plus 3 x the standard
570 deviation of negative control hamster sera.

571

572 *MesoPlex Assay*

573 The V-PLEX SARS-CoV-2 Panel 13 (IgG) kit from Meso Scale Discovery was used to test binding
574 antibodies against spike protein of SARS-CoV-2 with serum obtained from hamsters 14 DPI diluted at
575 10,000X. A standard curve of pooled hamster sera positive for SARS-CoV-2 spike protein was serially
576 diluted 4-fold. The secondary antibody was prepared by conjugating a goat anti-hamster IgG cross-
577 adsorbed secondary antibody (ThermoFisher) using the MSD GOLD SULFO-TAG NHS-Ester Conjugation
578 Pack (MSD). The secondary antibody was diluted 10,000X for use on the assay. The plates were prepped,
579 and samples were run according to the kit's instruction manual. After plates were read by the MSD
580 instrument, data was analyzed with the MSD Discovery Workbench Application.

581

582 *Virus neutralization*

583 Heat-inactivated γ -irradiated sera were two-fold serially diluted in DMEM. 100 TCID₅₀ of SARS-CoV-2 strain
584 England/204820464/2020 (B.1.1.7/Alpha, EPI_ISL_683466) or hCoV-19/USA/KY-CDC-2-4242084/2021
585 (B.1.617.2/Delta, EPI_ISL_1823618) was added. After 1 h of incubation at 37°C and 5% CO₂, the
586 virus:serum mixture was added to VeroE6 cells. CPE was scored after 5 days at 37°C and 5% CO₂. The
587 virus neutralization titer was expressed as the reciprocal value of the highest dilution of the serum that still
588 inhibited virus replication. The antigenic map was constructed as previously described [56, 57] using the
589 antigenic cartography software from <https://acmacs-web.antigenic-cartography.org>. In brief, this approach
590 to antigenic mapping uses multidimensional scaling to position antigens (viruses) and sera in a map to
591 represent their antigenic relationships. The maps here relied on the first SARS-CoV-2 infection serology
592 data of Syrian hamsters. The positions of antigens and sera were optimized in the map to minimize the
593 error between the target distances set by the observed pairwise virus-serum combinations. Maps were
594 effectively constructed in only one dimension because sera were only titrated against two viruses and the
595 dimensionality of the map is constrained to the number of test antigens minus one.

596

597 *Next-generation sequencing of virus*

598 Total RNA was extracted from oral swabs, lungs, and nasal turbinates using the Qia Amp Viral kit (Qiagen,
599 Germantown, MD), eluted in EB, and viral Ct values were calculated using real-time PCR. Subsequently,
600 11 µL of extracted RNA was used as a template in the ARTIC nCoV-2019 sequencing protocol V.1
601 (Protocols.io - <https://www.protocols.io/view/ncov-2019-sequencing-protocol-bbmuik6w>) to generate 1st-
602 strand cDNA. Five microliters were used as template for Q5 HotStart Pol PCR (Thermo Fisher Sci,
603 Waltham, MA) together with 10 uM stock of a single primer pair from the ARTIC nCoV-2019 v3 Panel
604 (Integrated DNA Technologies, Belgium), specifically 76L_alt3 and 76R_alt0. Following 35 cycles and 55°C
605 annealing temperature, products were AmPure XP cleaned and quantitated with Qubit (Thermo Fisher Sci)
606 fluorometric quantitation per instructions. Following visual assessment of 1 µL on a Tape Station D1000
607 (Agilent Technologies, Santa Clara, CA), a total of 400 ng of product was taken directly into TruSeq DNA
608 PCR-Free Library Preparation Guide, Revision D (Illumina, San Diego, CA) beginning with the Repair Ends
609 step (q.s. to 60 µL with RSB). Subsequent cleanup consisted of a single 1:1 AmPure XP/reaction ratio and
610 all steps followed the manufacturer's instructions including the Illumina TruSeq CD (96) Indexes. Final
611 libraries were visualized on a BioAnalyzer HS chip (Agilent Technologies) and quantified using KAPA
612 Library Quant Kit - Illumina Universal qPCR Mix (Kapa Biosystems, Wilmington, MA) on a CFX96 Real-
613 Time System (BioRad, Hercules, CA). Libraries were diluted to 2 nM stock, pooled together in equimolar
614 concentrations, and sequenced on the Illumina MiSeq instrument (Illumina) as paired-end 2 X 250 base
615 pair reads. Because of the limited diversity of a single-amplicon library, 20% PhiX was added to the final
616 sequencing pool to aid in final sequence quality. Raw fastq reads were trimmed of Illumina adapter
617 sequences using cutadapt version 1.1227, then trimmed and filtered for quality using the FASTX-Toolkit
618 (Hannon Lab, CSHL). To process the ARTIC data, a custom pipeline was developed [58]. Fastq read pairs
619 were first compared to a database of ARTIC primer pairs to identify read pairs that had correct, matching
620 primers on each end. Once identified, the ARTIC primer sequence was trimmed off. Read pairs that did not
621 have the correct ARTIC primer pairs were discarded. Remaining read pairs were collapsed into one
622 sequence using AdapterRemoval [59] requiring a minimum 25 base overlap and 300 base minimum length,
623 generating ARTIC amplicon sequences. Identical amplicon sequences were removed, and the unique
624 amplicon sequences were then mapped to the SARS-CoV-2 genome ([MN985325.1](https://ncbi.nlm.nih.gov/nucl/MN985325.1)) using Bowtie2 [60].
625 Aligned SAM files were converted to BAM format, then sorted and indexed using SAMtools [61]. Variant
626 calling was performed using Genome Analysis Toolkit (GATK, version 4.1.2) HaplotypeCaller with ploidy
627 set to 2 [62]. Single nucleotide polymorphic variants were filtered for QUAL > 200 and quality by depth (QD)
628 > 20 and indels were filtered for QUAL > 500 and QD > 20 using the filter tool in bcftools, v1.9 [61].

629

630 *Histopathology*

631 Necropsies and tissue sampling were performed according to IBC-approved protocols. Tissues were fixed
632 for a minimum of 7 days in 10% neutral buffered formalin with 2 changes. Tissues were placed in cassettes
633 and processed with a Sakura VIP-6 Tissue Tek on a 12-hour automated schedule using a graded series of
634 ethanol, xylene, and ParaPlast Extra. Prior to staining, embedded tissues were sectioned at 5 μ m and dried
635 overnight at 42°C. Using GenScript U864YFA140-4/CB2093 NP-1 (1:1000), specific anti-CoV
636 immunoreactivity was detected using the Vector Laboratories ImPress VR anti-rabbit IgG polymer (# MP-
637 6401) as secondary antibody. The tissues were then processed using the Discovery Ultra automated
638 processor (Ventana Medical Systems) with a ChromoMap DAB kit Roche Tissue Diagnostics (#760-159).

639

640 *Statistical Analysis*

641 Significance tests were performed as indicated where appropriate for the data using GraphPad Prism 9.
642 Unless stated otherwise, statistical significance levels were determined as follows: ns = $p > 0.05$; * = $p \leq$
643 0.05; ** = $p \leq 0.01$; *** = $p \leq 0.001$; **** = $p \leq 0.0001$. Exact nature of tests is stated where appropriate.

644

645 *Data availability statement*

646 Data to be deposited in Figshare.

647

648 **Acknowledgements**

649 We would like to thank Ryan Stehlik, Seth Cooley and Shanda Sarchette, and the animal care takers for
650 their assistance during the study. The following reagent was obtained through BEI Resources, NIAID, NIH:
651 SARS-CoV-2 variant Alpha (B.1.1.7) (hCoV320 19/England/204820464/2020, EPI_ISL_683466) and
652 variant Delta (B.1.617.2/) (hCoV-19/USA/KY-CDC-2-4242084/2021, EPI_ISL_1823618). We thank Neeltje
653 van Doremalen, Emmie de Wit, Brandi Williamson, Sujatha Rashid, Ranjan Mukul, Kimberly Stemple, Bin
654 Zhou, Natalie Thornburg, Sue Tong, Stacey Ricklefs, Sarah Anzick for gracefully sharing viruses or
655 propagating and sequencing stocks. We would like to thank Amy Tillman for assistance with the
656 aerodynamic particle data analysis.

657

658 **Funding**

659 This work was supported by the Intramural Research Program of the National Institute of Allergy and
660 Infectious Diseases (NIAID), National Institutes of Health (NIH) (1ZIAAI001179-01). JOL-S and DHM were
661 supported by the Defense Advanced Research Projects Agency DARPA PREEMPT (D18AC00031), the
662 UCLA AIDS Institute and Charity Treks, the 3Rs Pilot Studies program of the UCLA Animal Research
663 Committee, and the U.S. National Science Foundation (DEB-1557022). This work was part of NIAIDs
664 SARS-CoV-2 Assessment of Viral Evolution (SAVE) Program.

665

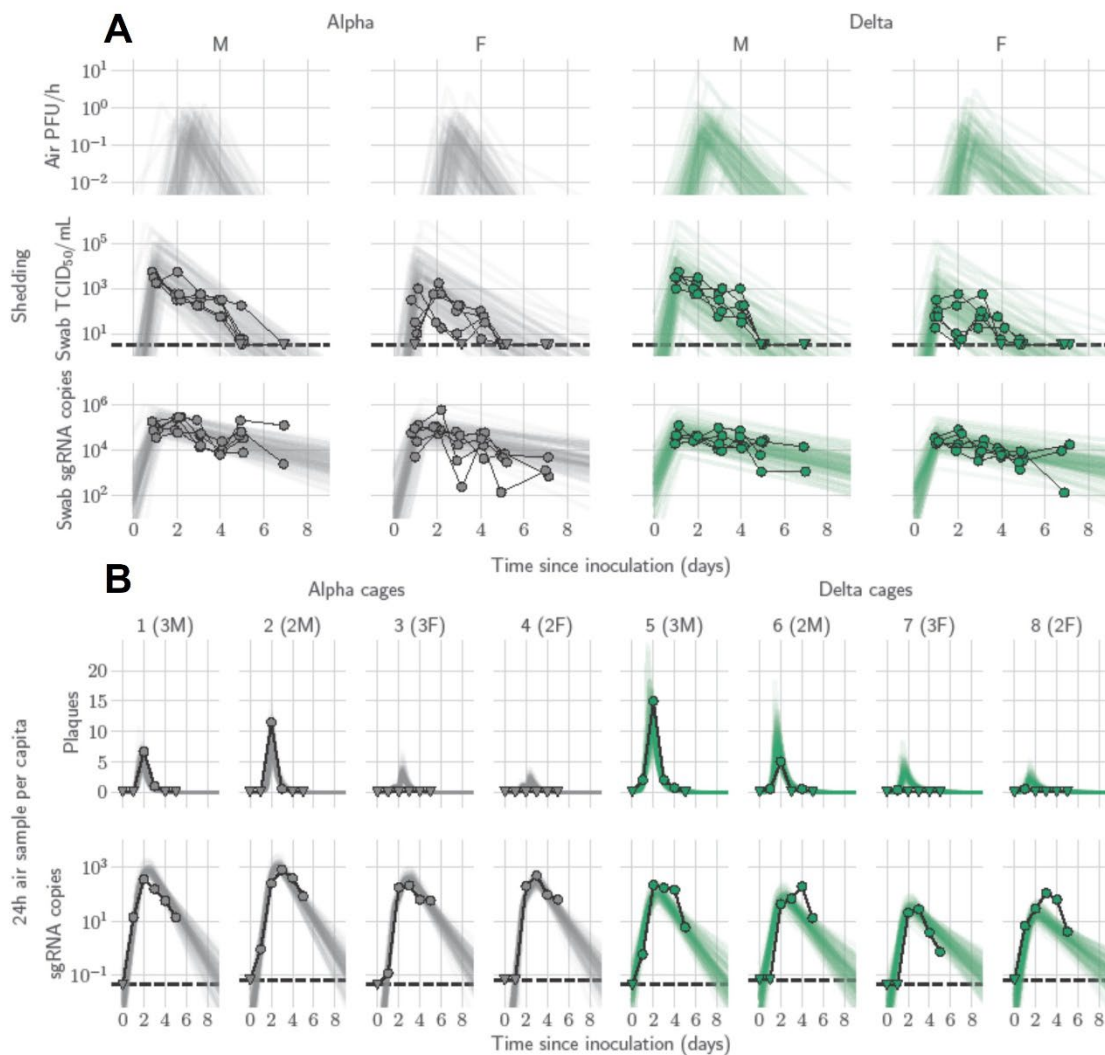
666 **References**

- 667 1. Zhang, R., et al., *Identifying airborne transmission as the dominant route for the spread of*
668 *COVID-19*. Proc Natl Acad Sci U S A, 2020. **117**(26): p. 14857-14863.
- 669 2. Port, J.R., et al., *Increased small particle aerosol transmission of B.1.1.7 compared with SARS-*
670 *CoV-2 lineage A in vivo*. Nature Microbiology, 2022. **7**(2): p. 213-223.
- 671 3. Boone, S.A. and C.P. Gerba, *Significance of Fomites in the Spread of Respiratory and Enteric*
672 *Viral Disease*. Applied and Environmental Microbiology, 2007. **73**(6): p. 1687-1696.
- 673 4. Goldman, E., *Exaggerated risk of transmission of COVID-19 by fomites*. Lancet Infect Dis, 2020.
674 **20**(8): p. 892-893.
- 675 5. CDC, *How COVID-19 Spreads*. 2021.
- 676 6. Pitol, A.K. and T.R. Julian, *Community Transmission of SARS-CoV-2 by Surfaces: Risks and*
677 *Risk Reduction Strategies*. Environmental Science & Technology Letters, 2021. **8**(3): p. 263-269.
- 678 7. CDC. *SARS-CoV-2 Variant Classifications and Definitions*. 2021 [cited 2021 18 January 2022].
- 679 8. Morawska, L., et al., *Size distribution and sites of origin of droplets expelled from the human*
680 *respiratory tract during expiratory activities*. Journal of Aerosol Science, 2009. **40**(3): p. 256-269.
- 681 9. Stadnytskyi, V., et al., *The airborne lifetime of small speech droplets and their potential*
682 *importance in SARS-CoV-2 transmission*. Proceedings of the National Academy of Sciences,
683 2020. **117**(22): p. 11875-11877.
- 684 10. Johnson, G.R. and L. Morawska, *The mechanism of breath aerosol formation*. J Aerosol Med
685 Pulm Drug Deliv, 2009. **22**(3): p. 229-37.
- 686 11. Coleman, K.K., et al., *Viral Load of Severe Acute Respiratory Syndrome Coronavirus 2 (SARS-*
687 *CoV-2) in Respiratory Aerosols Emitted by Patients With Coronavirus Disease 2019 (COVID-19)*
688 *While Breathing, Talking, and Singing*. Clinical Infectious Diseases, 2021.
- 689 12. Edwards, D.A., et al., *Exhaled aerosol increases with COVID-19 infection, age, and obesity*.
690 Proceedings of the National Academy of Sciences, 2021. **118**(8): p. e2021830118.
- 691 13. Milton, D.K., et al., *Influenza Virus Aerosols in Human Exhaled Breath: Particle Size, Culturability,*
692 *and Effect of Surgical Masks*. PLOS Pathogens, 2013. **9**(3): p. e1003205.
- 693 14. Sun, K., et al., *Transmission heterogeneities, kinetics, and controllability of SARS-CoV-2*.
694 Science, 2021. **371**(6526): p. eabe2424.
- 695 15. Yang, Q., et al., *Just 2% of SARS-CoV-2 positive individuals carry 90% of the virus*
696 *circulating in communities*. Proceedings of the National Academy of Sciences, 2021. **118**(21): p.
697 e2104547118.
- 698 16. Goyal, A., et al., *Viral load and contact heterogeneity predict SARS-CoV-2 transmission and*
699 *super-spreading events*. eLife, 2021. **10**: p. e63537.
- 700 17. Muñoz-Fontela, C., et al., *Animal models for COVID-19*. Nature, 2020. **586**(7830): p. 509-515.
- 701 18. Sia, S.F., et al., *Pathogenesis and transmission of SARS-CoV-2 in golden hamsters*. Nature,
702 2020. **583**(7818): p. 834-838.
- 703 19. Rosenke, K., et al., *Defining the Syrian hamster as a highly susceptible preclinical model for*
704 *SARS-CoV-2 infection*. Emerg Microbes Infect, 2020. **9**(1): p. 2673-2684.
- 705 20. Port, J.R., et al., *SARS-CoV-2 disease severity and transmission efficiency is increased for*
706 *airborne compared to fomite exposure in Syrian hamsters*. Nat Commun, 2021. **12**(1): p. 4985.
- 707 21. Port, J.R., et al., *Increased small particle aerosol transmission of B.1.1.7 compared with SARS-*
708 *CoV-2 lineage A in vivo*. Nature Microbiology, 2022.
- 709 22. Ganti, K., et al., *Timing of exposure is critical in a highly sensitive model of SARS-CoV-2*
710 *transmission*. PLOS Pathogens, 2022. **18**(3): p. e1010181.
- 711 23. Port, J.R., et al., *High-Fat High-Sugar Diet-Induced Changes in the Lipid Metabolism Are*
712 *Associated with Mildly Increased COVID-19 Severity and Delayed Recovery in the Syrian*
713 *Hamster*. Viruses, 2021. **13**(12): p. 2506.
- 714 24. Halfmann, P.J., et al., *SARS-CoV-2 Omicron virus causes attenuated disease in mice and*
715 *hamsters*. Nature, 2022. **603**(7902): p. 687-692.
- 716 25. Hawks, S.A., et al., *Infectious SARS-CoV-2 Is Emitted in Aerosol Particles*. mBio, 2021. **12**(5): p.
717 e0252721-e0252721.

- 718 26. Wang, C.C., et al., *Airborne transmission of respiratory viruses*. Science, 2021. **373**(6558): p.
719 eabd9149.
- 720 27. Jones, T.C., et al., *Estimating infectiousness throughout SARS-CoV-2 infection course*. Science,
721 2021. **373**(6551): p. eabi5273.
- 722 28. Kissler, S.M., et al., *Viral Dynamics of SARS-CoV-2 Variants in Vaccinated and Unvaccinated*
723 *Persons*. New England Journal of Medicine, 2021. **385**(26): p. 2489-2491.
- 724 29. Elie, B., et al., *Variant-specific SARS-CoV-2 within-host kinetics*. J Med Virol, 2022.
- 725 30. Earnest, R., et al., *Comparative transmissibility of SARS-CoV-2 variants Delta and Alpha in New*
726 *England, USA*. Cell Reports Medicine, 2022. **3**(4): p. 100583.
- 727 31. Hart, W.S., et al., *Generation time of the alpha and delta SARS-CoV-2 variants: an*
728 *epidemiological analysis*. The Lancet Infectious Diseases, 2022. **22**(5): p. 603-610.
- 729 32. Twohig, K.A., et al., *Hospital admission and emergency care attendance risk for SARS-CoV-2*
730 *delta (B.1.617.2) compared with alpha (B.1.1.7) variants of concern: a cohort study*. The Lancet
731 Infectious Diseases, 2022. **22**(1): p. 35-42.
- 732 33. Puhach, O., et al., *Infectious viral load in unvaccinated and vaccinated individuals infected with*
733 *ancestral, Delta or Omicron SARS-CoV-2*. Nature Medicine, 2022.
- 734 34. Snedden, C.E., et al., *SARS-CoV-2: Cross-scale Insights from Ecology and Evolution*. Trends in
735 Microbiology, 2021. **29**(7): p. 593-605.
- 736 35. Asadi, S., et al., *Non-respiratory particles emitted by guinea pigs in airborne disease transmission*
737 *experiments*. Scientific Reports, 2021. **11**(1): p. 17490.
- 738 36. Viklund, E., et al., *Severe acute respiratory syndrome coronavirus 2 can be detected in exhaled*
739 *aerosol sampled during a few minutes of breathing or coughing*. Influenza and Other Respiratory
740 Viruses, 2022. **16**(3): p. 402-410.
- 741 37. van Doremalen, N., et al., *ChAdOx1 nCoV-19 (AZD1222) or nCoV-19-Beta (AZD2816) protect*
742 *Syrian hamsters against Beta Delta and Omicron variants*. Nat Commun, 2022. **13**(1): p. 4610.
- 743 38. Ulrich, L., et al., *Enhanced fitness of SARS-CoV-2 variant of concern Alpha but not Beta*. Nature,
744 2022. **602**(7896): p. 307-313.
- 745 39. Achaiah, N.C., S.B. Subbarajasetty, and R.M. Shetty, *R(0) and R(e) of COVID-19: Can We*
746 *Predict When the Pandemic Outbreak will be Contained?* Indian J Crit Care Med, 2020. **24**(11): p.
747 1125-1127.
- 748 40. Ke, R., et al., *Estimating the reproductive number R0 of SARS-CoV-2 in the United States and*
749 *eight European countries and implications for vaccination*. Journal of Theoretical Biology, 2021.
750 **517**: p. 110621.
- 751 41. Liu, Y. and J. Rocklöv, *The reproductive number of the Delta variant of SARS-CoV-2 is far higher*
752 *compared to the ancestral SARS-CoV-2 virus*. J Travel Med, 2021. **28**(7).
- 753 42. Liu, Y. and J. Rocklöv, *The effective reproductive number of the Omicron variant of SARS-CoV-2*
754 *is several times relative to Delta*. J Travel Med, 2022. **29**(3).
- 755 43. Chen, P.Z., et al., *Heterogeneity in transmissibility and shedding SARS-CoV-2 via droplets and*
756 *aerosols*. Elife, 2021. **10**.
- 757 44. Majra, D., et al., *SARS-CoV-2 (COVID-19) superspreader events*. J Infect, 2021. **82**(1): p. 36-40.
- 758 45. Fukushi, S., et al., *Vesicular stomatitis virus pseudotyped with severe acute respiratory syndrome*
759 *coronavirus spike protein*. Journal of General Virology, 2005. **86**(8): p. 2269-2274.
- 760 46. Kawase, M., et al., *Protease-Mediated Entry via the Endosome of Human Coronavirus 229E*.
761 Journal of Virology, 2009. **83**(2): p. 712-721.
- 762 47. Letko, M., A. Marzi, and V. Munster, *Functional assessment of cell entry and receptor usage for*
763 *SARS-CoV-2 and other lineage B betacoronaviruses*. Nature Microbiology, 2020. **5**(4): p. 562-
764 569.
- 765 48. Takada, A., et al., *A system for functional analysis of Ebola virus glycoprotein*. Proceedings of the
766 National Academy of Sciences, 1997. **94**(26): p. 14764-14769.
- 767 49. Wrobel, A.G., et al., *SARS-CoV-2 and bat RaTG13 spike glycoprotein structures inform on virus*
768 *evolution and furin-cleavage effects*. Nature Structural & Molecular Biology, 2020. **27**(8): p. 763-
769 767.

- 770 50. Han, P., et al., *Molecular insights into receptor binding of recent emerging SARS-CoV-2 variants*.
771 Nature Communications, 2021. **12**(1): p. 6103.
- 772 51. Phan, D., N. Pradhan, and M. Jankowiak, *Composable effects for flexible and accelerated*
773 *probabilistic programming in NumPyro*. arXiv preprint arXiv:1912.11554, 2019.
- 774 52. Hoffman, M.D. and A. Gelman, *The No-U-Turn sampler: adaptively setting path lengths in*
775 *Hamiltonian Monte Carlo*. J. Mach. Learn. Res., 2014. **15**(1): p. 1593-1623.
- 776 53. Corman, V.M., et al., *Detection of 2019 novel coronavirus (2019-nCoV) by real-time RT-PCR*.
777 Euro Surveill, 2020. **25**(3).
- 778 54. Corman, V.M., et al., *Detection of 2019 novel coronavirus (2019-nCoV) by real-time RT-PCR*.
779 Euro surveillance : bulletin Europeen sur les maladies transmissibles = European communicable
780 disease bulletin, 2020. **25**(3): p. 2000045.
- 781 55. Yinda, C.K., et al., *K18-hACE2 mice develop respiratory disease resembling severe COVID-19*.
782 PLoS Pathog, 2021. **17**(1): p. e1009195.
- 783 56. Smith, D.J., et al., *Mapping the Antigenic and Genetic Evolution of Influenza Virus*. Science,
784 2004. **305**(5682): p. 371-376.
- 785 57. Fonville, J.M., et al., *Antibody landscapes after influenza virus infection or vaccination*. Science,
786 2014. **346**(6212): p. 996-1000.
- 787 58. Avanzato, V.A., et al., *Case Study: Prolonged Infectious SARS-CoV-2 Shedding from an*
788 *Asymptomatic Immunocompromised Individual with Cancer*. Cell, 2020. **183**(7): p. 1901-1912.e9.
- 789 59. Schubert, M., S. Lindgreen, and L. Orlando, *AdapterRemoval v2: rapid adapter trimming,*
790 *identification, and read merging*. BMC Res Notes, 2016. **9**: p. 88.
- 791 60. Langmead, B. and S.L. Salzberg, *Fast gapped-read alignment with Bowtie 2*. Nat Methods, 2012.
792 **9**(4): p. 357-9.
- 793 61. Li, H., et al., *The Sequence Alignment/Map format and SAMtools*. Bioinformatics, 2009. **25**(16): p.
794 2078-9.
- 795 62. McKenna, A., et al., *The Genome Analysis Toolkit: a MapReduce framework for analyzing next-*
796 *generation DNA sequencing data*. Genome Res, 2010. **20**(9): p. 1297-303.

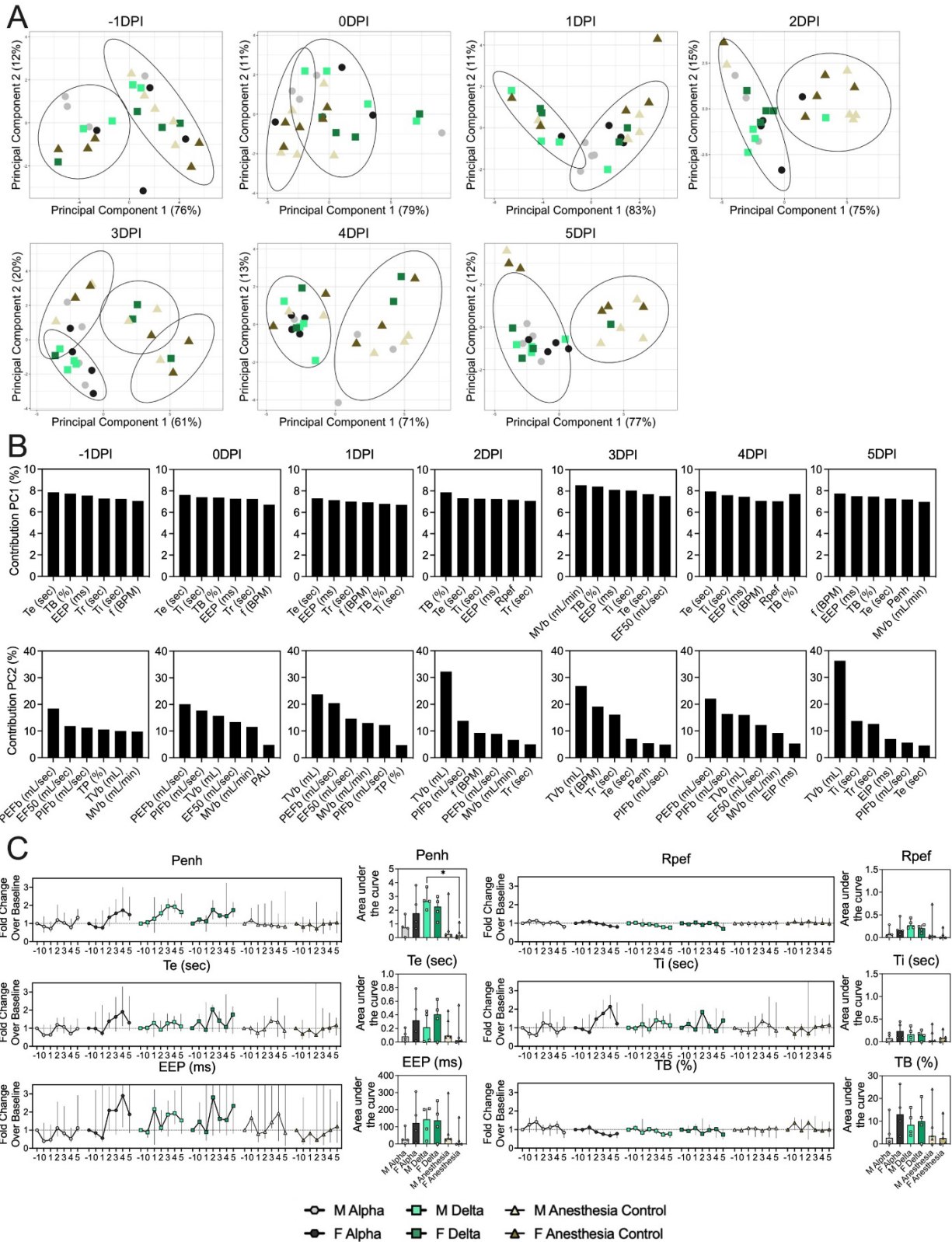
797



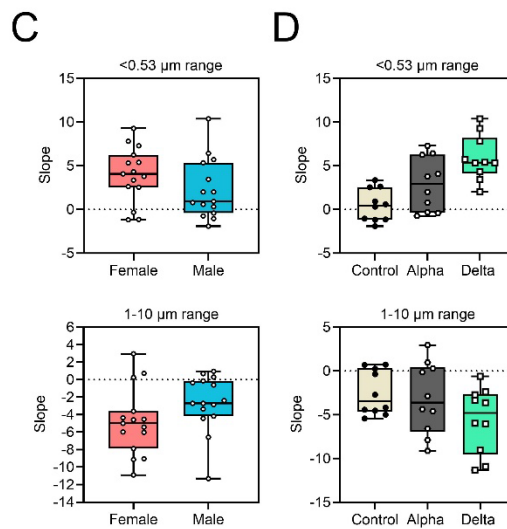
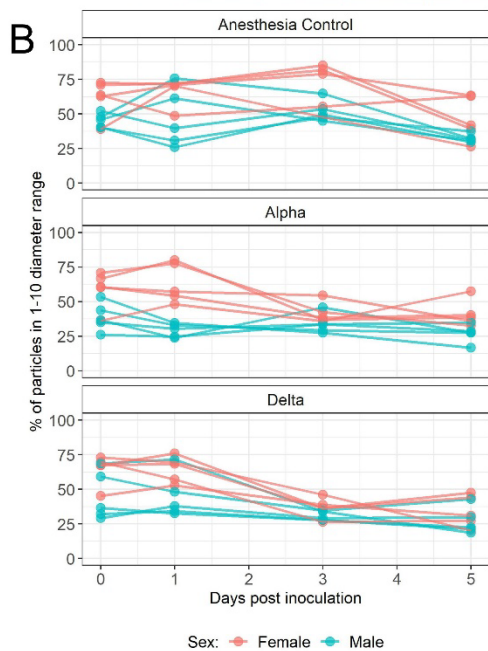
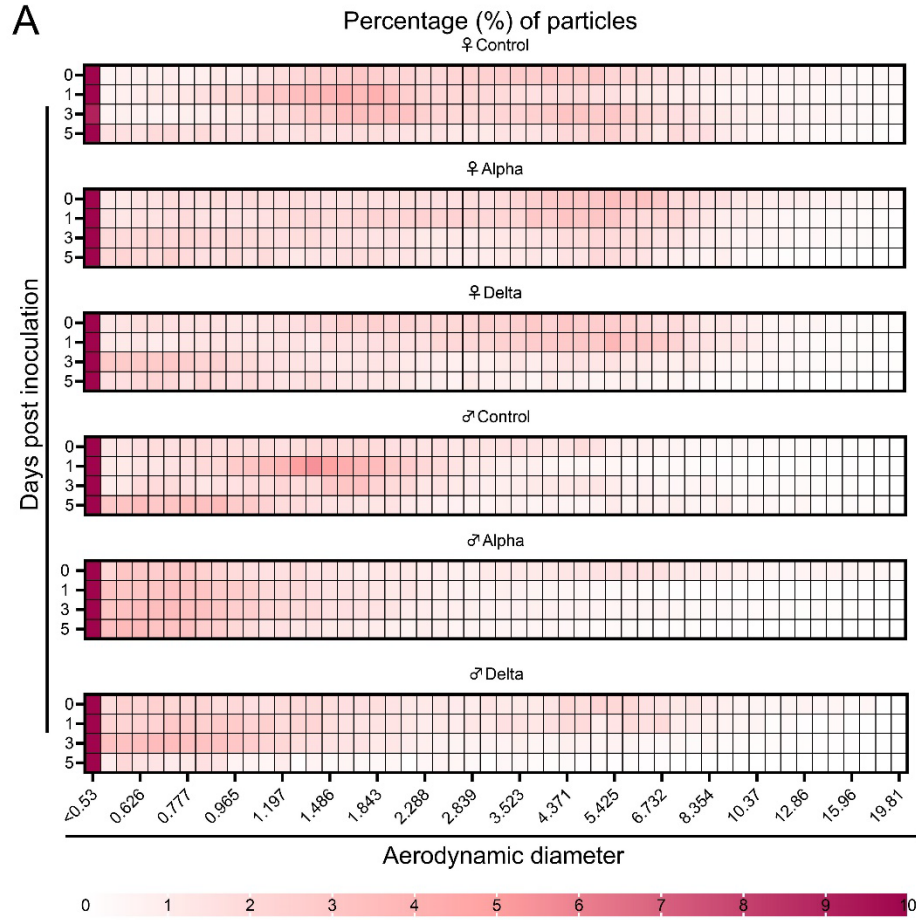
798

799 **Figure 1. Alpha and Delta variant shedding profiles in oral swabs and air samples.** Syrian hamsters
800 were inoculated with 10^3 TCID₅₀ via the intranasal route with Alpha or Delta. **A.** Comparison of swab viral
801 load and virus shedding into the air. Inferred profile of air shedding in PFU/h compared to sgRNA levels
802 and infectious virus titers (TCID₅₀/mL) in oropharyngeal swabs collected 1, 2, 3, 4, 5, and 7 DPI.
803 Semitransparent lines are 100 random draws from the inferred posterior distribution of hamster within-host
804 kinetics for each of the metrics. Joined points are individual measured timeseries for experimentally infected
805 hamsters; each set of joined points is one individual. Measurements and inferences shown grouped by
806 variant and animal sex. Measurement points are randomly jittered slightly along the x (time) axis to avoid
807 overplotting. **B.** Viral sgRNA and infectious virus (PFU) recovered from cage air sample filters over a 24 h
808 period starting at 0, 1, 2, 3, 4, and 5 DPI. Points are measured values, normalized by the number of
809 hamsters in the cage (2 or 3) to give per-capita values. Downward-pointing arrows represent virus below
810 the limit of detection (0 observed plaques or estimated copy number corresponding to Ct \geq 40).
811 Semitransparent lines are posterior predictions for the sample that would have been collected if sampling
812 started at that timepoint; these reflect the inferred underlying concentrations of sgRNA and infectious virus
813 in the cage air at each timepoint and are calculated from the inferred infection kinetics for each of the
814 hamsters housed within the cage. 100 random posterior draws shown for each cage. Cages housed 2 or 3
815 hamsters; all hamsters within a cage were of the same sex and infected with the same variant. Column

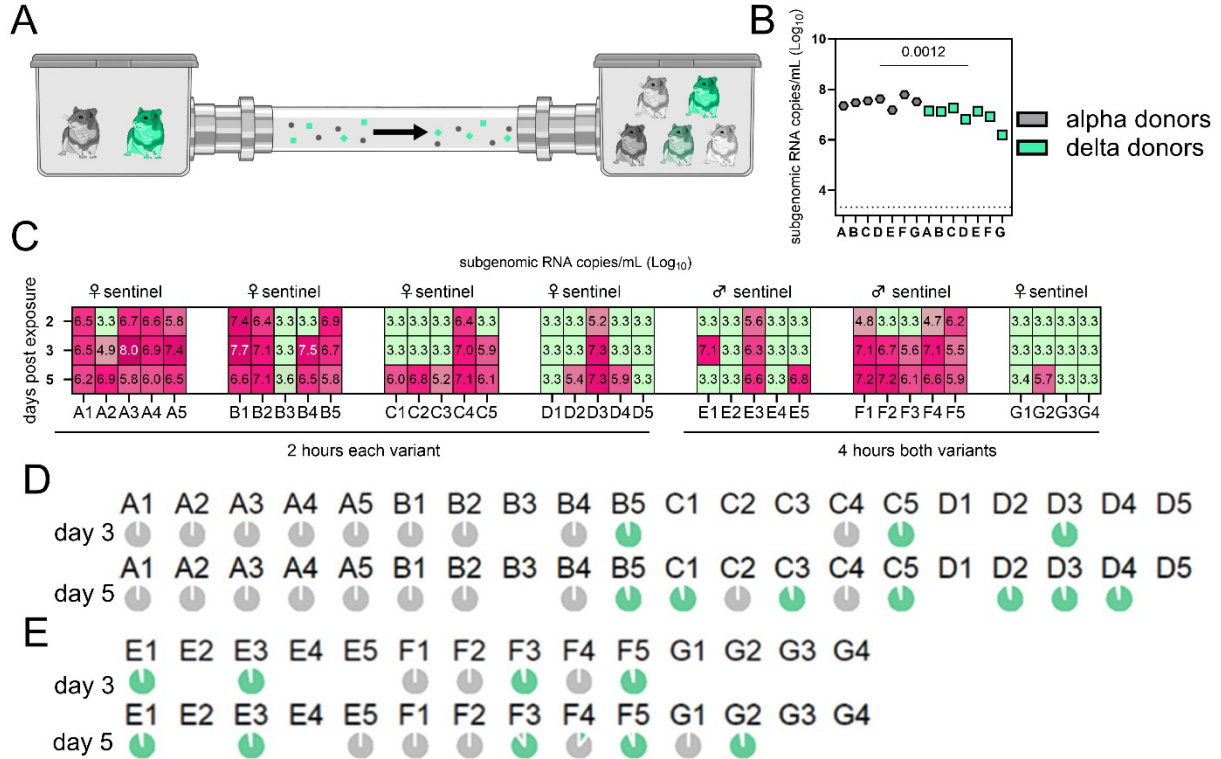
816 titles show cage number and variant, with number of and sex of individuals in parentheses. Dotted lines
817 limit of detection. Grey = Alpha, teal = Delta, p-values are indicated where significant. Abbreviations: sg,
818 subgenomic; TCID, Tissue Culture Infectious Dose; PFU, plaque forming unit; F, female; M, male; DPI,
819 days post inoculation.



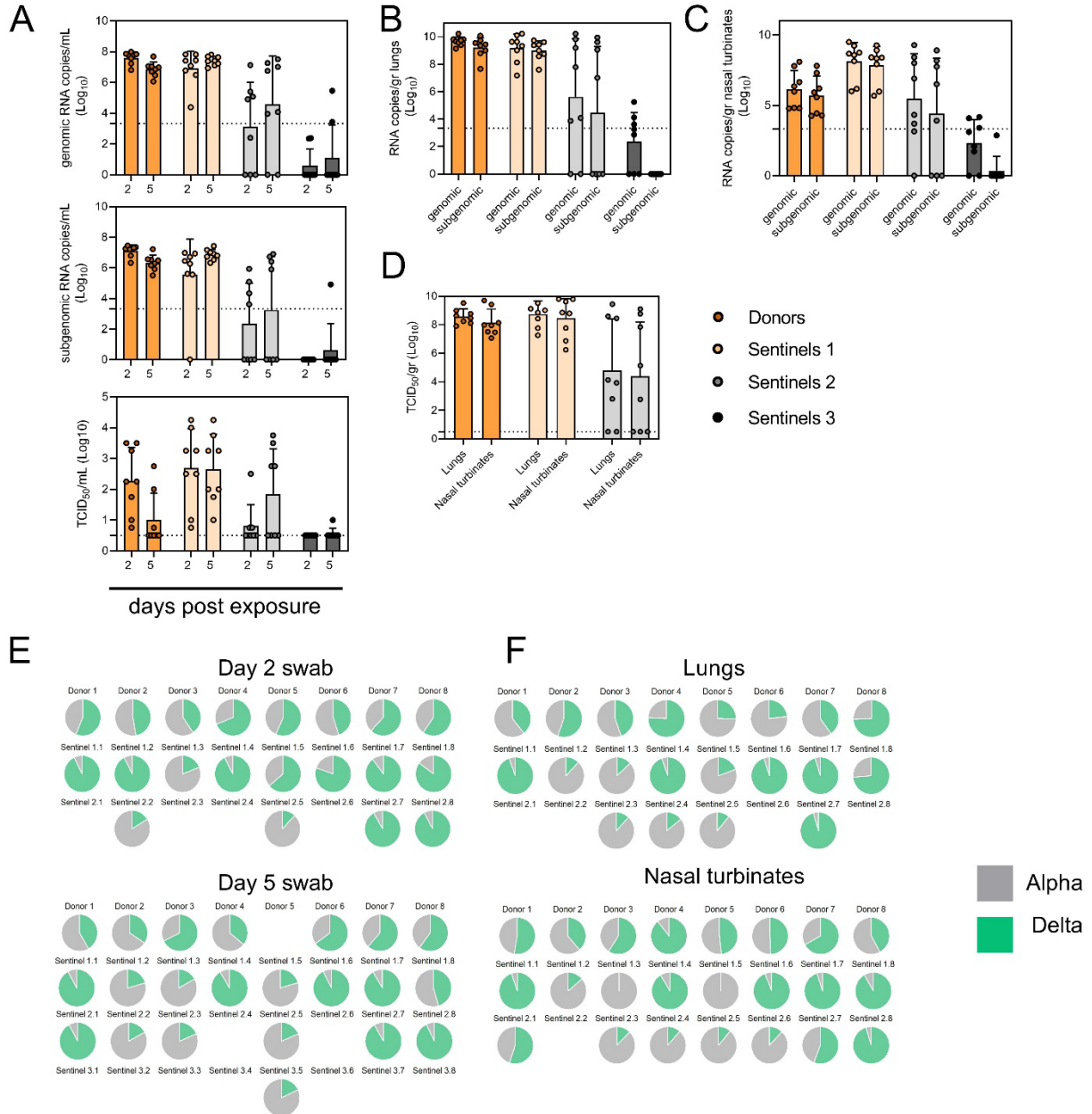
821 **Figure 2. Lung function and breathing changes after SARS-CoV-2 infection with Alpha and Delta.**
822 Syrian hamsters were inoculated with 10^3 TCID₅₀ via the intranasal route with Alpha or Delta. **A.** Lung
823 function was assessed on day -1, 0, 1, 2, 3, 4, and 5 by whole body plethysmography. Principal component
824 analysis was used to investigate individual variance. Depicted are principal component (PC) 1 and 2 for
825 each day, showing individual animals (colors refer to legend on right, sex-separated) and clusters (black
826 ellipses). **B.** Individual loading plots for contributions of top 6 variables to PC1 and 2 at each day. **C.**
827 Relevant subset of lung function parameters. Line graphs depicting median and 95% CI fold change values
828 (left) and area under the curve (AUC, right), Kruskal-Wallis test, p-values indicated where significant. Grey
829 = Alpha, teal = Delta, beige = anesthesia control, light = male, dark = female. Abbreviations: Expiratory time
830 (Te), inspiratory time (Ti), percentage of breath occupied by the transition from inspiration to expiration
831 (TB), end expiratory pause (EEP), breathing frequency (f), peak inspiratory flow (PIFb), peak expiratory
832 flow (PEFb), tidal volume (TVb), minute volume (MVb), enhanced pause (Penh), male (M), female (F).
833



835 **Figure 3: Aerodynamic particle analysis of SARS-CoV-2 infected hamsters. A.** Syrian hamsters were
836 inoculated with 10^3 TCID₅₀ via the intranasal route with Alpha or Delta. Aerodynamic diameter profile of
837 exhaled particles was analyzed on day 0, 1, 3, and 5. Heatmap shows rounded median percent of total
838 particles across groups, including the anesthesia control group (N = 10, comprising 5 males and 5 females).
839 Colors refer to scale below. **B.** For each animal, line graph of the percent of particles in the 1-10 μm diameter
840 range by variant group and sex indicated by color. **C/D.** Individual slopes for percent of particles in the
841 <0.53 μm range (top) and 1-10 μm range (bottom) are presented by sex and variant group. Boxplots depict
842 median, interquartile range, and range. Multiple linear regression performed for each diameter range with
843 group and sex as predictors, F-statistic (3,26) = 9.47 for <0.53 μm model and F-statistic (3,26) = 2.62 for 1-
844 10 μm model, with Tukey multiple comparison adjustment for the three variant-group comparisons (95%
845 family-wise confidence level). For <0.53 range, Male-Female (estimate = -1.7, standard error = 0.888, two-
846 sided p = 0.0659); Alpha-Control (estimate = 2.41, standard error = 1.09, two-sided p = 0.0874), Delta-
847 Control (estimate = 5.40, standard error = 1.09, two-sided p = 0.0001), Delta-Alpha (estimate = 2.99,
848 standard error = 1.09, two-sided p = 0.0280). For 1-10 range, Male-Female (estimate = 2.19, standard error
849 = 1.23, two-sided p = 0.0875); Alpha-Control (estimate = -0.633, standard error = 1.51, two-sided p =
850 0.9079), Delta-Control (estimate = -3.098, standard error = 1.51, two-sided p = 0.1197), Delta-Alpha
851 (estimate = -2.465, standard error = 1.51, two-sided p = 0.2498). Grey = Alpha, teal = Delta, beige =
852 anesthesia control, red = female, blue = male.
853



854
855 **Figure 4. Airborne attack rate of Alpha and Delta SARS-CoV-2 variants.** Donor animals (N = 7) were
856 inoculated with either the Alpha or Delta variant with 10^3 TCID₅₀ via the intranasal route and paired together
857 randomly (1:1 ratio) in 7 attack rate scenarios (A-G). To each pair of donors, one day after inoculation, 4-5
858 sentinels were exposed for a duration of 4 hours (i.e., hours 24-28 post inoculation) in an aerosol
859 transmission set-up at 200 cm distance. **A.** Schematic figure of the transmission set-up. **B.** Day 1 sgRNA
860 detected in oral swabs taken from each donor after exposure ended. Individuals are depicted. Wilcoxon
861 test, N = 7. Grey = Alpha, teal = Delta inoculated donors. **C.** Respiratory shedding measured by viral load
862 in oropharyngeal swabs; measured by sgRNA on day 2, 3, and 5 for each sentinel. Animals are grouped
863 by scenario. Colors refer to legend on right. 3.3 = limit of quality. **D/E.** Percentage of Alpha and Delta
864 detected in oropharyngeal swabs taken at day 2 and day 5 post exposure for each individual determined
865 by deep sequencing. Pie-charts depict individual animals. Grey = Alpha, teal = Delta.
866



867
868 **Figure 5. Airborne competitiveness of Alpha and Delta SARS-CoV-2 variants.** Donor animals (N = 8)
869 were inoculated with Alpha and Delta variant with 5×10^2 TCID₅₀, respectively, via the intranasal route (1:1
870 ratio), and three groups of sentinels (Sentinels 1, 2, and 3) were exposed subsequently at a 16.5 cm
871 distance. Animals were exposed at a 1:1 ratio; exposure occurred on day 1 (Donors → Sentinels 1) and
872 day 2 (Sentinels → Sentinels). **A.** Respiratory shedding measured by viral load in oropharyngeal swabs;
873 measured by gRNA, sgRNA, and infectious titers on days 2 and day 5 post exposure. Bar-chart depicting
874 median, 96% CI and individuals, N = 8, ordinary two-way ANOVA followed by Šidák's multiple comparisons
875 test. **B/C/D.** Corresponding gRNA, sgRNA, and infectious virus in lungs and nasal turbinates sampled five
876 days post exposure. Bar-chart depicting median, 96% CI and individuals, N = 8, ordinary two-way ANOVA,

877 followed by Šídák's multiple comparisons test. Dark orange = Donors, light orange = Sentinels 1, grey =
878 Sentinels 2, dark grey = Sentinels 3, p-values indicated where significant. Dotted line = limit of quality. **E.**
879 Percentage of Alpha and Delta detected in oropharyngeal swabs taken at days 2 and day 5 post exposure
880 for each individual donor and sentinel, determined by deep sequencing. Pie-charts depict individual
881 animals. Grey = Alpha, teal = Delta. **F.** Lung and nasal turbinate samples. Abbreviations: TCID, Tissue
882 Culture Infectious Dose.